

Ring Artifact Reduction via Multiscale Nonlocal Collaborative Filtering of Spatially Correlated Noise

Ymir Mäkinen,^{a*} Stefano Marchesini^b and Alessandro Foi^a

^aTampere University, Finland, and ^bSLAC National Accelerator Laboratory 2575 Sand Hill Road, Menlo Park, CA 94025. Correspondence e-mail: ymir.makinen@tuni.fi

X-ray micro-tomography systems often suffer severe ring artifacts in reconstructed images. These artifacts are caused by defects in the detector, calibration errors, and fluctuations producing streak noise in the raw sinogram data. We model these streaks in sinogram domain as additive stationary correlated noise upon logarithmic transformation. Based on this model, we propose a streak removal procedure where Block-Matching and 3-D (BM3D) filtering algorithm is applied across multiple scales, achieving state-of-the-art performance in both real and simulated data. Specifically, the proposed fully automatic procedure allows for attenuation of streak noise and the corresponding ring artifacts without creating major distortions common to other streak removal algorithms.

© 0000 International Union of Crystallography

1. Introduction

Ring artifacts are ubiquitous in computed tomography (Jha *et al.*, 2013; Artul, 2013; Boas & Fleischmann, 2012); they originate from angular streak noise in measured raw sinogram data used to reconstruct a tomographic volume (Croton *et al.*, 2019) and appear as darker or lighter circles or arcs centered on the axis of rotation for data acquisition. Streak noise can be caused by mis-calibration of detector linear response, beam fluctuations, beam hardening, or dusty or damaged scintillator screens (Haibel, 2008; Vidal *et al.*, 2005; Anas *et al.*, 2010).

Minimization of ring artifacts by using adequate scanning protocols (Pelt & Parkinson, 2018), high quality scintillator screens and detectors is possible. It is, however, difficult to completely avoid such artifacts and therefore achieve highest quality reconstruction solely by experimental measures. Several algorithms have been proposed to reduce ring artifacts in tomographic imaging, including wavelet-FFT filters (Münch *et al.*, 2009), combinations of polynomial smoothing filters and careful calibration of detector response function (Vo *et al.*, 2018; Croton *et al.*, 2019), or iterative algorithms (Paleo & Mirone, 2015) that combine regularized reconstruction with denoising.

In this work, we model the streak noise as a spatially correlated noise in sinogram domain, and propose a denoising procedure aiming to remove the streak noise before reconstruction. The denoising procedure is based on collaborative filtering, which employs both non-local self-similarity and transform-domain shrinkage to denoise a noisy signal through jointly transformed grouped blocks. In particular, we use the image denoising algorithm BM3D (Dabov *et al.*, 2007; Dabov *et al.*, 2008), leveraging the recent inclusion of exact transform-domain noise variances (Mäkinen *et al.*, 2020), which allow for accurate modeling of long noise correlation within the jointly transformed blocks.

Noting that some streaks may be too wide to be adequately captured by a group of standard-sized BM3D blocks, we further

propose multiscale streak removal with BM3D. The proposed procedure is fully automatic and includes self-calibration of the filtering strength. We demonstrate the superior performance of the proposed approach on real data from the table-top Prisma XRM microCT at Sigray, and from the Synchrotron based microCT at the Advanced Photon Source (APS) in Argonne, available through Tomobank (De Carlo *et al.*, 2018).

2. Transform-domain collaborative filtering of correlated noise

In this section, we interpret sinogram streaks as spatially correlated noise, formalizing streak removal as filtering of correlated noise where the streaks follow a basic stationary model. As a powerful tool to deal with this model, we adopt a recent BM3D designed for dealing with long-range correlation such as that which characterizes the streaks. This constitutes the denoising module at the core of a multiscale and nonstationary filtering architecture that will be presented in Section 3 for the more general case of real-world streak noise.

2.1. Correlated noise model

We consider a noisy input $z: X \rightarrow \mathbb{R}$ to be a combination of underlying data y and additive stationary spatially correlated noise η to be filtered:

$$z(x) = y(x) + \eta(x), \quad x \in X, \quad (1)$$

where $x \in X \subset \mathbb{Z}^2$ is the coordinate in the finite two-dimensional image domain X (representing angles and displacements when z is a sinogram) and

$$\eta = \nu \circledast g, \quad \nu(\cdot) \sim \mathcal{N}(0, 1), \quad (2)$$

ν being zero-mean i.i.d. Gaussian noise with unit variance, and \circledast denoting 2-D convolution with the kernel g . The kernel g defines the spatial correlation of the noise as well as the noise

strength, with $\|g\|_2 = \text{std}(\eta)$. An equivalent way of representing correlated noise is by its power spectral density (PSD) Ψ :

$$\Psi = \mathbb{E} \left\{ |\mathcal{F}[\eta]|^2 \right\} = \text{var} \{ \mathcal{F}[\eta] \} = |X| |\mathcal{F}[g]|^2, \quad (3)$$

with \mathcal{F} being the 2-D Fourier transform, and $|X|$ denoting the cardinality (i.e. number of elements) of X . Equivalently, a kernel g satisfying (2)-(3) can be defined from Ψ as

$$g = |X|^{-1/2} \mathcal{F}^{-1} [\text{std}(\mathcal{F}[\eta])] = |X|^{-1/2} \mathcal{F}^{-1} [\sqrt{\Psi}]. \quad (4)$$

2.1.1. Basic model for constant stationary streaks. Although the streaks are originally multiplicative in nature, sinogram data is considered upon a logarithmic transformation and therefore the streaks can be modeled by the additive noise η in (1). The sinogram streak noise is fairly constant in the angular dimension, presenting very long-range correlation in the noise along this dimension. Treating angle as the vertical dimension and displacement as horizontal, we consider the basic case of horizontally white and vertically constant streak noise. Such noise can be modeled through (2), when setting g as a vertically constant line. This simple kernel as well as the corresponding PSD Ψ are demonstrated in Figure 1; an example of real streak noise viably approximated through this model is shown in Figure 2.

In practice, the above simple model cannot be used but for small segments of the sinograms, as streak noise can often feature horizontal correlation, vertical variations, or nonstationarities that are not described by the model. In Section 3, a complete processing pipeline is further proposed to allow modeling more complex cases of streak noise through (1)-(4), enabling their attenuation through the collaborative filter.

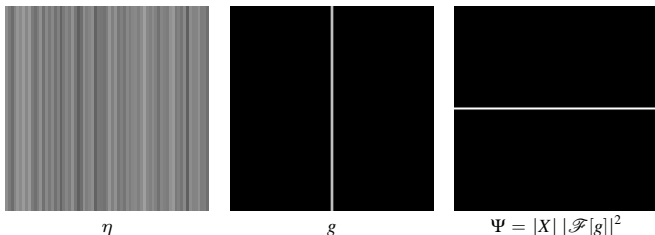


Figure 1
Example noise $\eta = \nu \otimes g$, $\nu(\cdot) \sim \mathcal{N}(0, 1)$, the corresponding correlation kernel g , and PSD Ψ . For the kernel and the PSD, black pixels of the image correspond to value 0 in the data.

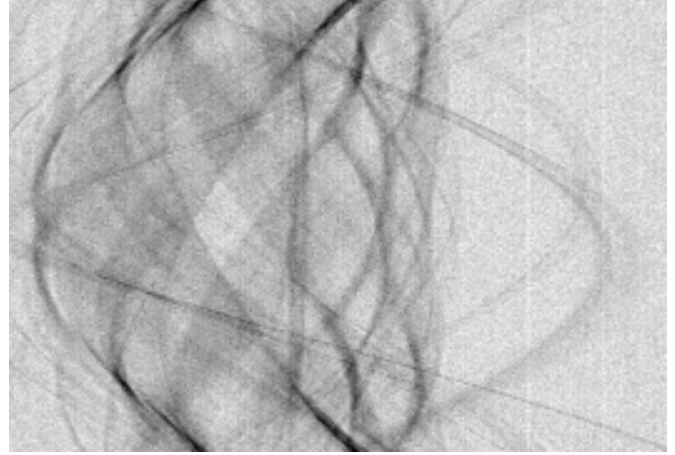


Figure 2
Example of streak noise in a sinogram (a fragment of *Fly*) that can be seen as well approximated by the model in Figure 1.

2.2. Transform-domain collaborative filtering and BM3D

The rationale of transform-domain filtering is to work with a representation of the signal where most of the signal is compacted to only a few coefficients, whereas the remaining coefficients are mostly comprised of noise. Hence, by attenuating the coefficients with a non-linear shrinkage operator, it is possible to attenuate noise while keeping most of the signal intact. Nonlocal collaborative filters utilize this property in the context of collective transform coefficients of groups of similar blocks extracted from the image. In all of the following sections, we consider the recently proposed variant (Mäkinen *et al.*, 2020) of BM3D for correlated noise denoising where the input is z and the goal of denoising is to estimate y based on the statistics of η or equivalently knowledge of Ψ or g .

In BM3D, all operations are made with regard to a reference block moving through the image. For each position of the reference block, the following steps are executed:

1. Collect similar blocks into a group through **block-matching**
2. Obtain the 3-D transform spectrum by collectively transforming the obtained blocks
3. Perform **shrinkage**
4. Transform the shrunk spectra back to block estimates and **aggregate** them to the original locations from which they were collected

The 3-D transform spectrum of the grouped noisy blocks is obtained through first applying a 2-D transform \mathcal{T}^{2D} locally to each block, then a 1-D transform \mathcal{T}^{NL} through the "stack" of grouped blocks. Denoting by $\{z_{x_1}, \dots, z_{x_M}\}$ a group of M blocks of N pixels extracted from z at coordinates x_1, \dots, x_M , we obtain the \mathcal{T}^{2D} spectrum coefficients as $s_i^x = \langle z_{x_t}, b_i^{2D} \rangle$, for $i = 1, \dots, N$, $t = 1, \dots, M$, where b_i^{2D} is the i -th basis function of \mathcal{T}^{2D} . The 3-D spectrum coefficients are calculated through

the direct tensor product of the \mathcal{T}^{2D} and \mathcal{T}^{NL} transforms, as

$$\begin{aligned} s_{i,j}^{x_1, \dots, x_M} &= \langle [z_{x_1}; \dots; z_{x_M}], b_i^{2D} \otimes b_j^{NL} \rangle = \\ &= \langle [s_i^{x_1}, \dots, s_i^{x_M}], b_j^{NL} \rangle = \sum_{t=1}^M b_j^{NL}(t) s_i^{x_t}, \end{aligned} \quad (5)$$

where $b_j^{NL}(t)$ is the t -th element of the j -th basis function b_j^{NL} of \mathcal{T}^{NL} , \otimes denotes the tensor product, and $[\cdot; \dots; \cdot]$ denotes the stacking of the blocks along the 3rd dimension. The indexing and notation of the transform spectrum coefficients are illustrated in Figure 3.

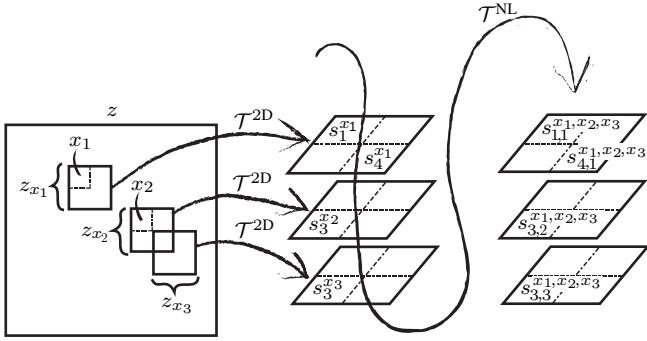


Figure 3

Notation and indexing of patch coordinates x_l , patches z_{x_l} , and coefficients $s_i^{x_l}$ and $s_{i,j}^{x_1, \dots, x_M}$ in the corresponding \mathcal{T}^{2D} spectra and \mathcal{T}^{3D} spectrum, reproduced with permission from Mäkinen *et al.* (2020). The illustration is for a group of three blocks of size 2×2 at coordinates $x_1 = (4, 3)$, $x_2 = (7, 5)$, $x_3 = (8, 6)$ within a 10×10 -pixel image.

In each step of the algorithm, the variances of $s_{i,j}^{x_1, \dots, x_M}$ play a key role; we denote them by $v_{i,j}^{x_1, \dots, x_M}$. For their calculation, we refer the reader to Mäkinen *et al.* (2020). Here, we provide a summary of the macroscopic operations of the algorithm.

2.2.1. Block-matching. For each reference block, BM3D defines a local neighborhood from which similar blocks are collected. Each block in the neighborhood is ranked by

$$L_{x_R}(x_j) = \|z_{x_R} - z_{x_j}\|_2^2 - 2\gamma \sum_{i=1}^N v_{i,2}^{x_R, x_j}, \quad (6)$$

where z_{x_R} is the reference block, z_{x_j} is a potential match, $v_{i,2}^{x_R, x_j}$ is the i -th coefficient of the block-pair transform-domain variance corresponding to block difference, and $\gamma \in \mathbb{R}$. The common aim of block-matching is to find blocks which are the most similar to the reference block in terms of the underlying noise-free content. When only a noisy image is available, the similarity is evaluated between noisy blocks and the term scaled by γ in (6) compensates for bias in the ranking caused by noise correlation. Specifically, with $\gamma = 0$ the matches would be mainly guided by the strong vertical correlation of the streak noise and thus be located along the streaks, largely ignoring any similarity of the underlying signal; setting $\gamma > 0$ mitigates this bias by promoting matching of blocks in which the noise is not correlated with that of the reference block. In particular, we employ

$\gamma = 3$ as proposed by Mäkinen *et al.* (2020) for the general case of correlated noise, facilitating further the matching of blocks which differ from the reference block mainly due to the variance of the block difference.

The common design of BM3D includes two distinct stages of denoising with different shrinkage operators, meaning that the full image is processed twice. In the second stage, the block-matching is commonly executed on the image estimate produced by the first denoising stage. As this image can be presumed noise-free, the second block-matching is executed without any compensation for noise correlation.

2.2.2. Shrinkage of the 3-D spectra. The core of BM3D is shrinkage performed on the 3-D transform spectrum of the grouped noisy blocks. For a given transform-domain coefficient of the group, a generic shrinkage can be expressed as

$$s_{i,j}^{x_1, \dots, x_M} \mapsto \alpha_{i,j} s_{i,j}^{x_1, \dots, x_M}, \quad (7)$$

where $\alpha_{i,j}$ is a shrinkage attenuation factor which depends on $s_{i,j}^{x_1, \dots, x_M}$, the noise statistics, and possible other priors.

BM3D utilizes two shrinkage operations: in the first denoising stage, the denoising process performs shrinkage by hard-thresholding; the second stage employs a Wiener filter, utilizing the hard-thresholding image estimate as a pilot signal.

In hard-thresholding, the shrinkage is performed by setting spectrum coefficients smaller than a threshold to zero, as they are mostly composed of noise:

$$\alpha_{i,j}^{\text{HT}} = \begin{cases} 1 & \text{if } |s_{i,j}^{x_1, \dots, x_M}| \geq \sqrt{v_{i,j}^{x_1, \dots, x_M}} \lambda \\ 0 & \text{otherwise,} \end{cases} \quad (8)$$

where $\lambda \geq 0$ is a fixed constant.

In Wiener filtering, the attenuation coefficients of the transfer function are computed from the previous estimate, used as pilot signal, and from the variance of the noise spectrum coefficients as

$$\alpha_{i,j}^{\text{W}} = \frac{\| \langle [\hat{y}_{x_1}^{\text{HT}}, \dots, \hat{y}_{x_M}^{\text{HT}}], b_i^{2D} \otimes b_j^{NL} \rangle \|^2}{\| \langle [\hat{y}_{x_1}^{\text{HT}}, \dots, \hat{y}_{x_M}^{\text{HT}}], b_i^{2D} \otimes b_j^{NL} \rangle \|^2 + \mu^2 v_{i,j}^{x_1, \dots, x_M}}, \quad (9)$$

where \hat{y}^{HT} is the estimate of y obtained from the hard-thresholding stage, and μ^2 is a scaling factor included due to aggregation to influence the bias-variance ratio we wish to minimize through the Wiener filter.

2.2.3. Aggregation. After calculating the attenuation factors of the group, they can be applied to the 3-D transform spectra to obtain estimates for the grouped blocks:

$$\hat{y}_{x_j} = Q^{2D} \left\{ \left\langle \alpha_{i,j}^{x_1, \dots, x_M} s_{i,j}^{x_1, \dots, x_M}, q_j^{NL} \right\rangle \right\}, \quad (10)$$

where Q^{2D} is the inverse transform of \mathcal{T}^{2D} , and q_j^{NL} is the j -th transform basis function of the inverse of \mathcal{T}^{NL} .

Hence, an estimate is produced for all blocks included in the group. As a new group is built for every position x_R of the reference block, there is a large amount of block estimates providing a highly redundant covering of the image. Let X_R be the set

of coordinates of all reference blocks and denote by $\{\hat{y}_{x_j}^{x_R}\}_{j=1}^{M_{x_R}}$ the set of estimates (10) for the group of blocks matched to the reference block at position x_R . Then, the block estimates of an image are $\bigcup_{x_R \in X_R} \{\hat{y}_{x_j}^{x_R}\}_{j=1}^{M_{x_R}}$ and they can all be distinct.

We aggregate all block estimates at their respective positions into the image through an adaptive weighted average

$$\hat{y} = \frac{\sum_{x_R \in X_R} \sum_{j=1}^{M_{x_R}} \omega_{x_j}^{x_R} W_{x_j} \hat{y}_{x_j}^{x_R}}{\sum_{x_R \in X_R} \sum_{j=1}^{M_{x_R}} \omega_{x_j}^{x_R} W_{x_j}}, \quad (11)$$

where $\omega_{x_j}^{x_R}$ is a block-specific weight and W_{x_j} is a windowing function over blocks at position x_j . The weights $\omega_{x_j}^{x_R}$, inversely proportional to the residuals of transform-domain noise variances, promote estimates with less residual noise to improve quality of the final estimate.

The steps for denoising a group of blocks are demonstrated in Figure 4.

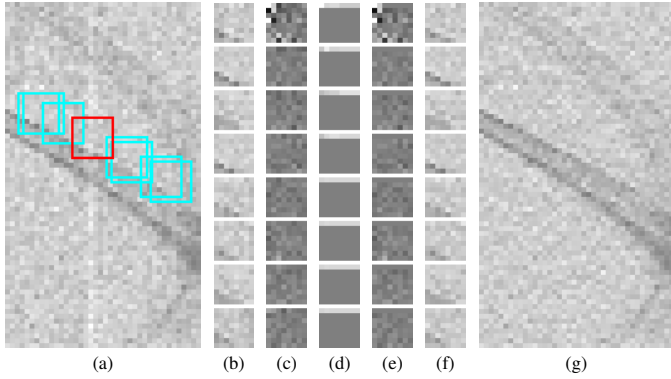


Figure 4

Denoising a part of *Fly* (a portion of Figure 2) with vertical streak noise with Ψ as in Figure 1. Left to right: (a) Positions x_1, \dots, x_8 of one group of blocks with reference block in red; (b) contents of the 8 matched blocks z_{x_1}, \dots, z_{x_8} ; (c) the resulting \mathcal{T}^{3D} spectrum coefficients $s_{i,j}^{x_1, \dots, x_8}$; (d) corresponding 3-D noise standard deviations $\sqrt{v_{i,j}^{x_1, \dots, x_8}}$; (e) hard-thresholded coefficients $\alpha_{i,j}^{HT} s_{i,j}^{x_1, \dots, x_8}$; (f) the denoised group of blocks $\hat{y}_{x_1}^{HT}, \dots, \hat{y}_{x_8}^{HT}$, and (g) the denoising result of hard-thresholding \hat{y}^{HT} . For the spectrum coefficients and the standard deviations (c,d,e), 50%-gray pixel color in the figure corresponds to value 0 in the data.

3. Processing pipeline

In this section, we consider the necessary steps for modeling the streak noise through (1) for real sinogram data, hence allowing the effective application of BM3D for streak removal.

3.1. Bright-fielding and log-transformation

The optical attenuation through the sample is determined experimentally via bright-field corrections requiring two additional inputs, the bright-field and the dark-field (Seibert *et al.*, 1998). The bright-field is an acquisition obtained by the imaging procedure with no sample, and the dark-field is obtained with no beam; both are 2-D arrays the size of effective pixels

of the detector. Furthermore, the Beer-Lambert law relates the X-ray transform through the sample to the optical attenuation by a logarithmic transformation (Swinehart, 1962).

Hence, the raw projections P_{raw} are first normalized as

$$P_{\text{norm}} = \frac{P_{\text{raw}} - I_D}{I_B - I_D}, \quad (12)$$

where I_D is the dark-field and I_B is the bright-field¹, and then log-transformed as

$$P_{\text{log}} = \ln(P_{\text{norm}}). \quad (13)$$

Bright-fielding (12) provides a partial, but not thorough correction of the streak noise (Davidson *et al.*, 2003); the denoising pipeline of the following sections is designed to attenuate the remaining streak noise.

3.1.1. Noise in the projections. Apart from possible completely defective detectors² we treat the variation in detector response as normally distributed. We further model the streak noise as locally stationary, meaning that the streak variance is presumed constant within sufficient area (i.e. the block-matching search neighborhood) for the application of BM3D. As the data is obtained through a photon-counting detector, the statistics of the measured raw data can be further modeled through a Poisson distribution. Considering both the approximately normally distributed streak noise and the Poissonian component, noise in projections normalized by (12) can be modeled as

$$P_{\text{norm}} = A(1 + \eta_p) + \pi = \left(A + \frac{\pi}{1 + \eta_p} \right) (1 + \eta_p), \quad (14)$$

where A are the noise-free projections, η_p is the normally distributed streak noise component, and π is (approximately) white Poissonian noise with zero mean; all components of (14) are considered as 3-D arrays and multiplications are elementwise.

We note that the natural logarithm of (13) acts as a variance-stabilizing transformation for the multiplicative noise component $(1 + \eta_p)$. Hence, we have

$$P_{\text{log}} = \ln(P_{\text{norm}}) \approx \ln\left(A + \frac{\pi}{1 + \eta_p}\right) + \eta_p, \quad (15)$$

where the approximation comes from $\ln(1 + \eta_p) \approx \eta_p$. The additive noise component η_p in (15) corresponds to the streak noise to be denoised. As here we only aim to attenuate the streak noise, through denoising we estimate $\ln\left(A + \frac{\pi}{1 + \eta_p}\right)$; the embedded noise term $\frac{\pi}{1 + \eta_p}$ although not i.i.d. is nevertheless (approximately) white and does not present streaks.

Individual sinograms, each of which is defined as a cross-section of the stack of projections P_{log} , are denoted as

$$Z = Y + \eta_z, \quad (16)$$

where Y denotes the underlying streak-free sinogram, and η_z is the corresponding cross-section of η_p . The sinograms Z are used as the input for the processes in the following Section 3.2.

¹ As P_{raw} is a 3-D array, the pixels of I_B and I_D are replicated through the angle dimension for the operations in (12).

² Extreme streak noise arising from defective detectors is addressed separately in Section 3.4.

3.2. Multiscale filtering architecture

In what follows, we assume that sinograms Z are oriented such that streaks are oriented vertically, i.e. the angular component is vertical and the displacement is horizontal.

The streak noise η_z is characterized by very long-range correlation. In particular, because vertically there are no high-frequency streak noise components, the streaks can be filtered entirely at a *coarse vertical scale*, with consequent benefits in terms of efficacy and computational efficiency. Furthermore, BM3D operates using blocks of fixed size within a limited neighborhood which may be too small to fully denoise the wider streaks. Thus, we also want to denoise across *multiple horizontal scales* to effectively attenuate streaks of varying sizes.

Our multiscale implementation is based on a simple and efficient pixel binning to go towards coarser scales by replacing adjacent pixels by their sum. To go back towards finer scales we leverage the iterative debinning approach from Azzari & Foi (2016), which is based on spline upsampling. The multiscale denoising process is illustrated in Figure 5 and proceeds as follows.

We begin with a single *vertical* binning of the full noisy sinogram Z of height m to a sinogram Z_0 of height $m_v \leq m$ through a binning operator \mathcal{B}_v . On Z_0 , we perform all consequent horizontal operations and denoising.

After vertical binning, the sinogram Z_0 is progressively halved in size K times through a *horizontal* binning operator $\mathcal{B}_h: Z_k = \mathcal{B}_h(Z_{k-1}) = \mathcal{B}_h^k(Z_0) = \mathcal{B}_h^k(\mathcal{B}_v(Z))$, $k = 1, \dots, K$. Denoting by n the width of Z and Z_0 , Z_k has width $\lceil 2^{-k}n \rceil$; with every binning, the streak width gets also halved. The multiscale denoising is operated in a coarse-to-fine fashion, where progressively for each $k = K, K-1, \dots, 2, 1, 0$, we obtain an estimate \hat{Y}_k of $\mathcal{B}_h^k(\mathcal{B}_v(Y))$. We start by taking as noisy input Z_K^* of BM3D the smallest binned sinogram Z_K ; in this way, we obtain from $Z_K^* = Z_K$ the coarsest estimate \hat{Y}_K , which is taken as initialization for the following recursive steps executed for each scale $k = K-1, \dots, 0$:

1. Replace the horizontal coarser-scale components of Z_k by those of the estimate \hat{Y}_{k+1} :

$$\begin{aligned} Z_k^* &= Z_k - \mathcal{B}_h^{-1}(\mathcal{B}_h(Z_k)) + \mathcal{B}_h^{-1}(\hat{Y}_{k+1}) \\ &= Z_k - \mathcal{B}_h^{-1}(Z_{k+1} - \hat{Y}_{k+1}) . \end{aligned}$$

2. Denoise Z_k^* with BM3D to produce the estimate \hat{Y}_k .

The result \hat{Y}_0 of the last denoising step is the fully denoised estimate the size of Z_0 . To produce the full-size estimate \hat{Y} of Y , we replace the vertical coarse-scale components of Z with those of \hat{Y}_0 , similar to the Step 1 above:

$$\hat{Y} = Z - \mathcal{B}_v^{-1}(\mathcal{B}_v(Z_0)) + \mathcal{B}_v^{-1}(\hat{Y}_0) = Z - \mathcal{B}_v^{-1}(Z_0 - \hat{Y}_0) .$$

Figure 6 illustrates the sinograms over the various stages of the multiscale denoising process.

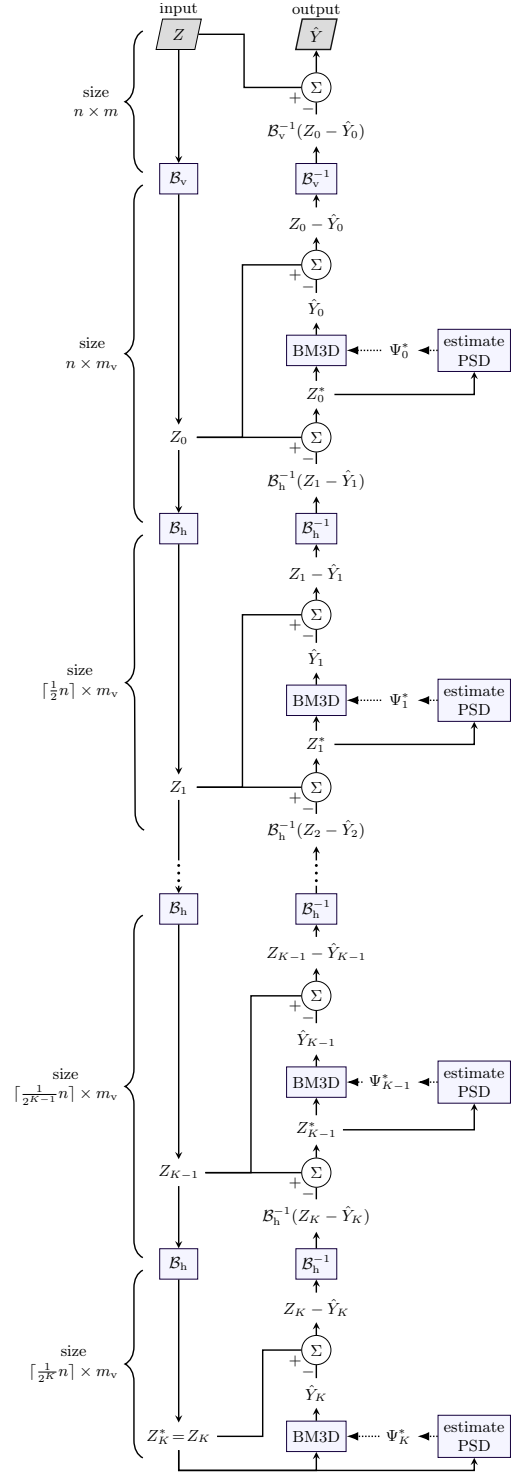


Figure 5

Flowchart of the multiscale denoising process, starting from the noisy sinogram Z and resulting in the estimate \hat{Y} of the streak-free sinogram, both of size $n \times m$. First, Z is vertically rescaled into a sinogram Z_0 of size $n \times m_v$, $m_v \leq m$, through the binning operator \mathcal{B}_v . Then, by repeated horizontal binning \mathcal{B}_h , Z_0 is progressively downscaled into a series of sinograms $Z_k = \mathcal{B}_h(Z_{k-1})$, $k = 1, \dots, K$, each of size $\lceil 2^{-k}n \rceil \times m_v$. The coarsest scale noisy input $Z_K^* = Z_K$ is denoised with BM3D to produce \hat{Y}_K . Then, recursively for $k = K-1, \dots, 0$, the noisy input $Z_k^* = Z_k - \mathcal{B}_h^{-1}(Z_{k+1} - \hat{Y}_{k+1})$ is denoised by BM3D to produce \hat{Y}_k ; this definition of Z_k^* means that the coarse-scale horizontal components of Z_k are replaced by \hat{Y}_{k+1} . The PSD for each scale is estimated as described in Section 3.3.2. The resulting estimate \hat{Y}_0 of the horizontal debinning (size $n \times m_v$) similarly replaces the coarse-scale vertical components of Z to obtain the full-size estimate \hat{Y} .

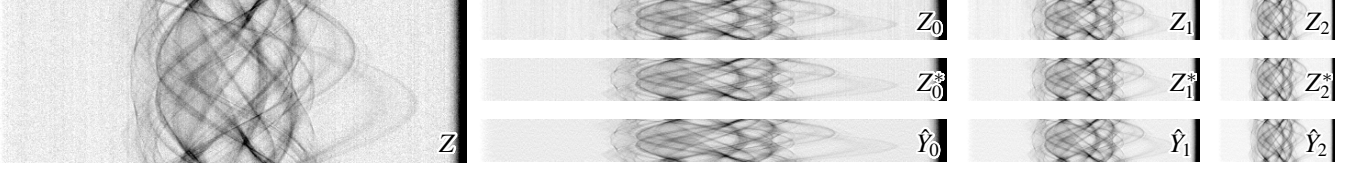


Figure 6

Multiscale denoising of *Fly*. Left: the noisy sinogram Z . Center and right: three scales of the multiscale denoising process, each showing Z_k , Z_k^* , and \hat{Y}_k . The full-size estimate \hat{Y} is displayed in Figure 12.

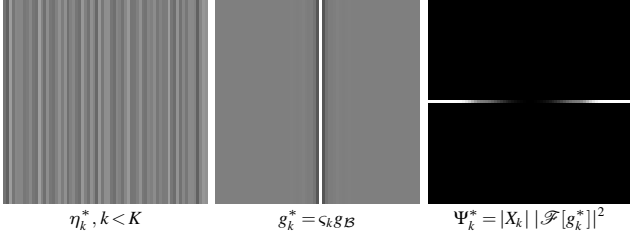


Figure 7

Example of noise η_k^* of Z_k^* , $k < K$, the correlation kernel $g_k^* = c_k g_B$ where g_B is produced by \mathcal{B} and \mathcal{B}^{-1} , and the corresponding PSD Ψ_k^* . For the kernel, 50%-gray pixel color in the figure corresponds to value 0 in the data; for the PSD, black is 0. Note the missing low frequencies at the center of the PSD, and the higher-frequency nature of η_k^* compared to the white streak noise η in Figure 1.

3.3. Multiscale noise model

For BM3D denoising, we regard Z_k^* of each scale k as z of the model (1), as

$$Z_k^* = \mathcal{B}_h^k(\mathcal{B}_v(Y)) + \eta_k^*, \quad (17)$$

where

$$\eta_k^* = \begin{cases} \eta_K & k = K, \\ \eta_k - \mathcal{B}_h^{-1}(\mathcal{B}_h(\eta_k)) & k < K, \end{cases} \quad (18)$$

and $\eta_k = \mathcal{B}_h^k(\mathcal{B}_v(\eta_z))$. This definition for η_k^* , $k < K$ follows from considering the coarser-scale estimate \hat{Y}_k as perfectly denoised. Similar to (3), η_k^* is treated as correlated noise with PSD

$$\Psi_k^* = \text{var}(\mathcal{F}[\eta_k^*]) = |X_k| |\mathcal{F}[g_k^*]|^2, \quad K \geq k \geq 0, \quad (19)$$

where g_k^* is a correlation kernel and $|X_k| = \lceil 2^{-k}n \rceil_{m_v}$. As per (4), the kernel g_k^* can be defined as

$$g_k^* = |X_k|^{-1/2} \mathcal{F}^{-1}[\text{std}(\mathcal{F}[\eta_k^*])]. \quad (20)$$

3.3.1. Multiscale PSD of white streak noise. Let $\eta_0 = \mathcal{B}_v(\eta_z)$ be horizontally white and vertically constant streak noise like in Figure 1. Under this assumption for η_0 , we have that also all $\eta_k = \mathcal{B}_h^k(\eta_0)$ for $0 \leq k \leq K$ are horizontally white and vertically constant, with variance $\text{var}(\eta_k) = 2^k \text{var}(\eta_0)$. The doubling of the variance with every horizontal binning follows from the noise whiteness, which means that each pixel of the coarser scale sinogram is a sum of two pixels with independent noise of equal variance. Therefore, disregarding the specific support size of their actual finite realizations, we can identify these stationary random fields as

$$\eta_k = 2^{k/2} \text{std}(\eta_0) \eta_W, \quad (21)$$

where η_W is a white streak noise like in Figure 1 with $\text{var}(\eta_W) = 1$. We can hence rewrite (18) as

$$\eta_k^* = \begin{cases} 2^{K/2} \text{std}(\eta_0) \eta_W & k = K \\ 2^{k/2} \text{std}(\eta_0) (\eta_W - \mathcal{B}_h^{-1}(\mathcal{B}_h(\eta_W))) & k < K. \end{cases} \quad (22)$$

This together with (20) means that we can characterize η_k^* through a kernel g_k^* obtained by scaling either of two basic two kernels g_c and g_B ,

$$\begin{aligned} g_c &= |X|^{-1/2} \mathcal{F}^{-1}[\text{std}(\mathcal{F}[\eta_W])], \\ g_B &= |X|^{-1/2} \mathcal{F}^{-1}[\text{std}(\mathcal{F}[\eta_W - \mathcal{B}_h^{-1}(\mathcal{B}_h(\eta_W))])], \end{aligned} \quad (23)$$

by a factor

$$c_k = 2^{k/2} \text{std}(\eta_0) = \text{std}(\eta_k), \quad (24)$$

as

$$g_k^* = \begin{cases} c_k g_c & k = K, \\ c_k g_B & k < K. \end{cases} \quad (25)$$

We note that although the equalities (23) formally depend on the realization size $|X|$, in practice this term only renormalizes the kernel with regard to the Fourier transforms; hence (23) can be computed for an arbitrary support.

The kernel g_c is single-pixel wide and vertically constant like in Figure 1, with $\|g_c\|_2 = \text{std}(\eta_W) = 1$. Example noise η_k^* , $k < K$, and the corresponding kernel $g_k^* = c_k g_B$ and PSD Ψ_k^* (19) are shown in Figure 7.

Estimation of c_0 . To estimate $\text{std}(\eta_0) = c_0$, we first convolve Z_0 with a 2-D kernel $g_d = \phi \otimes \psi$ where ϕ is a 1-D column Gaussian function of length $m_v/2$ and standard deviation $m_v/12$ and ψ is a horizontal high-pass Daubechies wavelet "db3" of length 6, hence convolution with g_d realizes low-pass filtering in vertical and high-pass filtering in horizontal. Thus, compared to Z_0 , $Z_0 \otimes g_d$ offers a lower signal-to-noise ratio (SNR), which facilitates the estimation of noise statistics; an example of Z_0 and the corresponding $Z_0 \otimes g_d$ are shown in Figure 8 (top). One can compute an estimate of the standard deviation of $\eta_0 \otimes g_d$ via its median absolute deviation (Hampel, 1974):

$$\widehat{\text{std}(\eta_0 \otimes g_d)} = 1.4826 \text{smed} \left(\left| Z_0 \otimes g_d - \text{smed}_{X_0}(Z_0 \otimes g_d) \right| \right), \quad (26)$$

where smed denotes the sample median and the factor 1.4826 calibrates the estimate with respect to a normal distribution of the noise. As $\text{std}(\eta_0 \otimes g_d) = \|c_0 g_c \otimes g_d\|_2$, an estimate \hat{c}_0 of c_0 can be obtained through

$$\hat{c}_0 = \|g_c \otimes g_d\|_2^{-1} \widehat{\text{std}(\eta_0 \otimes g_d)}. \quad (27)$$

3.3.2. Adapting the model to non-white streak noise. The above model (21)-(25) assumes that the streak noise η_z is horizontally white and stationary; however, real streak noise is never exactly white across the displacement, and may thus have significant differences in noise power between scales.

To adapt to these deviations from the model, we relax the definition (24) of ς_k and allow the scaling parameter $\varsigma_k \geq 0$ to vary with each scale k , while assuming the kernels as in (25) for simplicity³. In this way, to adaptively model the PSD (19), we require only the estimation of ς_k on each Z_k^* .

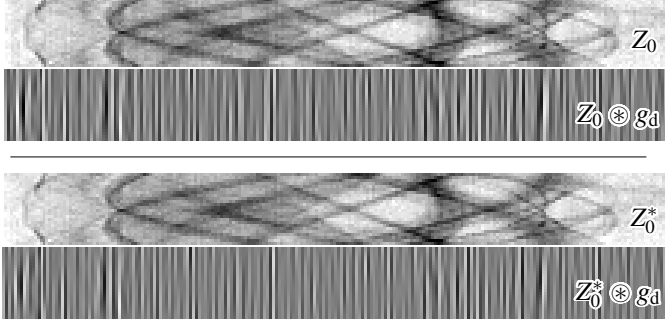


Figure 8

A fragment of Z_0 of *Fly* and the corresponding $Z_0 \otimes g_d$ (top), and a fragment of Z_0^* with the corresponding $Z_0^* \otimes g_d$ (bottom). For $Z_0 \otimes g_d$ and $Z_0^* \otimes g_d$, 50%-gray pixel color in the figure corresponds to value 0 in the data. Note how most of the signal of the sinogram fragments is not present in the convolved arrays, facilitating the estimation of the streak noise statistics. Although $Z_0 \otimes g_d$ and $Z_0^* \otimes g_d$ look very similar, careful visual inspection reveals slight differences similar to those between $\eta = \eta_k$ in Figure 1 and η_k^* in Figure 7.

Estimation of ς_k , $k \geq 0$. For $k = K$, ς_K can be estimated from $Z_K = Z_K^*$ by trivial substitutions of 0 with K in (26) and (27). Although also for $k < K$ one could estimate ς_k similarly from Z_k , a more accurate estimate can be obtained using Z_k^* as this leverages the denoising of the coarser scales and thus $Z_k^* \otimes g_d$ offers an even lower SNR than $Z_k \otimes g_d$. An example of Z_k^* and the corresponding $Z_k^* \otimes g_d$ are shown in Figure 8 (bottom). Similar to (26) and for any $K \geq k \geq 0$, the standard deviation of the noise in $Z_k^* \otimes g_d$ can be estimated as

$$\widehat{\text{std}(\eta_k^* \otimes g_d)} = 1.4826 \underset{x_k}{\text{smed}} \left(\left| Z_k^* \otimes g_d - \underset{x_k}{\text{smed}}(Z_k^* \otimes g_d) \right| \right).$$

Noting that $\text{std}(\eta_k^* \otimes g_d) = \|g_k^* \otimes g_d\|_2$, we then estimate ς_k as

$$\hat{\varsigma}_k = \begin{cases} \|g_c \otimes g_d\|_2^{-1} \widehat{\text{std}(\eta_K^* \otimes g_d)} & k = K, \\ \|g_B \otimes g_d\|_2^{-1} \widehat{\text{std}(\eta_k^* \otimes g_d)} & k < K. \end{cases} \quad (28)$$

3.3.3. Horizontal nonstationarity of η_z . Variance of the streak noise may differ across the sinogram due to changes in photon flux or noise in the bright-field. Thus, it may not be possible to denoise Z_k^* assuming a constant ς_k for all spatial positions without either oversmoothing or leaving noise artifacts

³ Adopting the kernels (25) with arbitrary values of ς_k corresponds to assuming η_k approximately white with variance ς_k^2 , which may differ from $2^k \text{std}(\eta_0)$ against (21). This assumption becomes increasingly appropriate as k grows for non-white η_0 featuring mild local horizontal correlations, as the binning in $\mathcal{B}_n^k(\eta_0)$ is tantamount to a convolution and decimation, leading to a flattening of the PSD.

in some areas. To adapt to horizontal nonstationarity, we further relax the model allowing ς_k to vary within each scale k . In particular, before noise estimation and denoising, we split Z_k^* and $Z_k^* \otimes g_d$ into overlapping, full-height segments. We apply BM3D separately on each segment of Z_k^* , using a PSD scaled by $\hat{\varsigma}_k$ estimated on the corresponding segment of $Z_k^* \otimes g_d$, i.e. we consider each segment as a separate noisy image z with a corresponding Ψ . After denoising, the segment estimates produced by BM3D are recombined with a windowing function to form the full estimate \hat{Y}_k .

3.4. Attenuation of extreme streaks

We note that the projections often include several streaks caused by defects in the scintillator. These streaks can be far stronger than what reasonably produced by the distribution of η_p and therefore require a specific pre-processing. To this end, after applying the bright-field and before the multiscale denoising process, we run a simple procedure on P_{\log} which aims to detect and attenuate only the most extreme streaks. First, we calculate the median across the angular dimension of the 3-D stack of projections as $\tilde{P} = \underset{\text{angle}}{\text{smed}}(P_{\log})$, resulting in a 2-D map in which the streaks present as pixels extremely brighter or darker than their surroundings. To detect extreme outliers, for each coordinate x representing a single pixel of the detector and hence of \tilde{P} , we fit a bivariate cubic polynomial \wp_x to a window \tilde{P}_x of \tilde{P} centered at x . Then, consistent with Gaussian modeling of η_p , we mark the center pixel $\tilde{P}(x)$ defective if $|\tilde{P}(x) - \wp_x(x)| > 4 \text{sstd}\{\tilde{P}_x - \wp_x\}$, where sstd denotes the sample standard deviation; each marked pixel in \tilde{P} corresponds to a full column of the sinograms.

Each pixel of a defective column is replaced with the median of non-defective pixels within a 2-D window considering the displacement dimensions around it. We note that columns corrected in this way are unlikely to be completely free of streak noise; instead, the aim is to introduce less extreme pixel values that can be further denoised by the following applications of BM3D. In order to not overload the notation, we denote the output of this step as P_{\log} identical to its input.

The complete streak noise attenuation procedure is illustrated in Figure 9. The procedure is fully automatic, requiring as an input only the raw projections and the bright- and dark-fields.

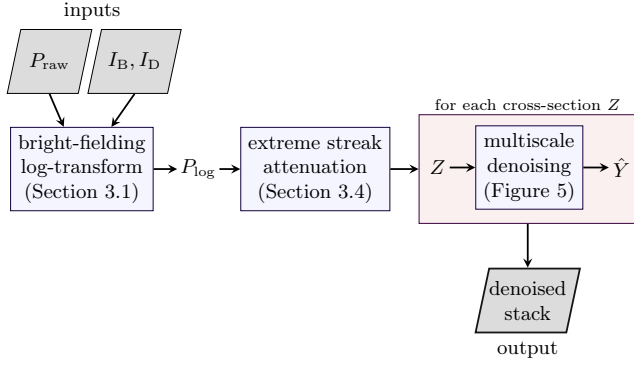


Figure 9

The complete denoising process, requiring as inputs the noisy projections P_{raw} and the bright- and dark-fields I_B, I_D , and producing as the output an estimate of the streak-free stack of projections composed of sinogram estimates \hat{Y} .

4. Experiments

We test our pipeline on synthetic data as well as two real acquisitions displaying ring artifacts. As a comparison, we show results for two leading streak-removal procedures from the *tomopy* library (Gürsoy *et al.*, 2014): Münch *et al.* (2009) and Vo *et al.* (2018). In particular, for the latter we combine "Algorithm 3", "Algorithm 5", and "Algorithm 6", which is demonstrated in Vo *et al.* (2018) to attenuate a variety of different streaks.

For the synthetic experiments, we use a sinogram (627×180 px) of the Shepp-Logan phantom obtained through MATLAB Radon transform upon a sign change and an exponential transformation. We regard this sinogram as the noise-free projections A and generate noise according to (14) with g as a one-pixel wide image-height vertical kernel like the one in Figure 1. To obtain streak noise of different strengths, the streak noise component $(1 + \eta_p)$ is generated with $\text{std}(\eta_p) = 0.005, 0.01, 0.02, 0.05$. Next, to generate noisy measurements with different SNR levels for the Poisson component, we separately scale A to the ranges $[1280, 2560]$ (higher SNR) and $[640, 1280]$ (lower SNR) and generate a Poisson variate with mean and variance $A(1 + \eta_p)$, thus defining the Poissonian noise π as the difference between this Poisson variate and $A(1 + \eta_p)$. Furthermore, we include experiments with $\pi = 0$ (infinite SNR), thus resulting in a total of 12 combinations of Poisson and streak noise strengths. We do not simulate extreme streaks. As the underlying data consists of only a single sinogram, we have $Z = P_{\text{log}}$ and we consider $\ln(A + \pi/(1 + \eta_p))$ as the streak-free sinogram Y . The results of the phantom experiments are collected in Table 1, and illustrated in Figure 10 and Figure 11.

Table 1

Average signal-to-noise ratio (SNR) after attenuation of streaks in the Shepp-Logan phantom subject to mixed streak and Poissonian noise as in (14), with different combinations of $\text{std}(\eta_p)$ and peak values of A , with $\text{peak} = \infty$ being the limiting case for which $\pi = 0$. As all of the algorithms aim to remove streak noise only, the SNR values are calculated with $Y = \ln(A + \pi/(1 + \eta_p))$ as $\text{SNR}(\hat{Y}) = 10 \log_{10} \left(\frac{\text{svar}\{Y^2\}}{\text{smean}\{(\hat{Y} - Y)^2\}} \right)$, where svar and smean denote sample variance and sample mean, respectively. Each value of the table is the average SNR over 10 different noise realizations.

peak	$\text{std}(\eta_p)$	SNR			
		noisy	Münch <i>et al.</i> (2009)	Vo <i>et al.</i> (2018)	proposed
∞ ($\pi = 0$)	0.005	32.61	11.80	28.97	44.05
	0.01	26.59	11.78	28.52	39.19
	0.02	20.58	11.72	27.48	34.29
	0.05	12.77	11.49	24.62	27.24
2560	0.005	32.66	11.85	28.32	38.41
	0.01	26.64	11.82	27.89	35.90
	0.02	20.63	11.77	26.90	32.63
	0.05	12.82	11.54	24.21	26.67
1280	0.005	32.71	11.90	27.76	36.51
	0.01	26.69	11.87	27.36	34.31
	0.02	20.68	11.82	26.45	31.55
	0.05	12.86	11.59	23.92	26.21

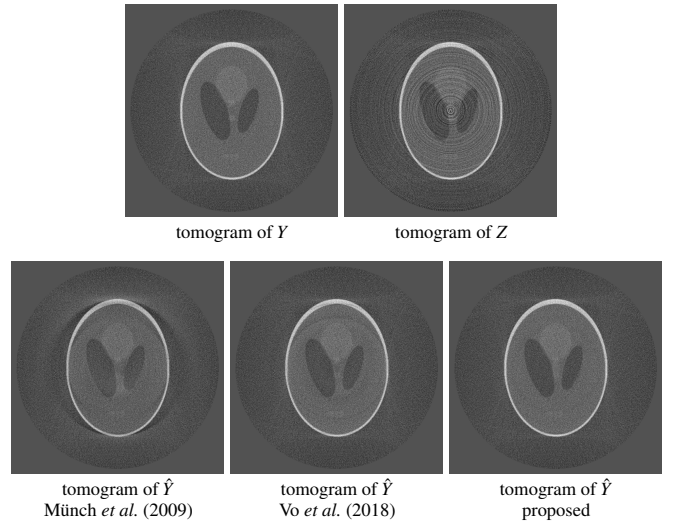


Figure 11

Corresponding tomograms of Figure 10. On top, $Y = \ln(A + \pi/(1 + \eta_p))$ and Z . On bottom, left-to-right, Münch *et al.* (2009), Vo *et al.* (2018), proposed procedure based on BM3D denoising. Note the strong circular components on both Münch *et al.* (2009) and Vo *et al.* (2018), not present in the noisy tomogram or in the proposed result.

The *Fly* dataset consists of 180 projections with 50 second exposure (detector pixel size 27 micron, demagnified to 15.7 microns by cone-beam geometry) collected using Sigray Prisma X-ray micro-tomography instrument at 34 kV; each sinogram is 512px wide. The *Fly* contains both extreme streaks caused by defective detectors and approximately normally distributed

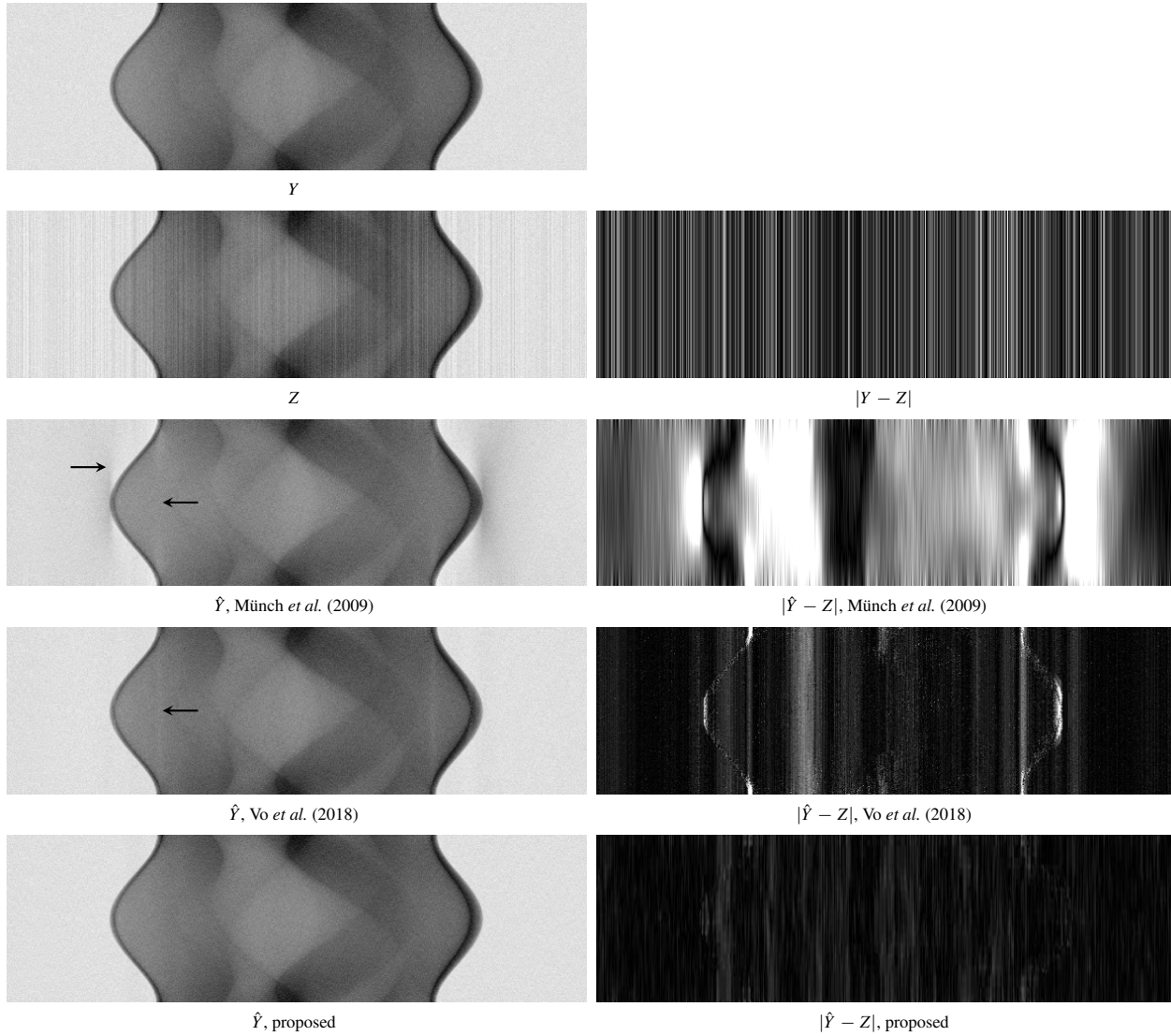


Figure 10

Left: Comparison of sinograms after different denoising procedures on the Shepp-Logan phantom with noise as in (14) with $\text{std}(\eta_p) = 0.02$ and signal peak 2560. Top to bottom: $Y = \ln(A + \pi/(1 + \eta_p))$, Z , Münch *et al.* (2009), Vo *et al.* (2018), proposed procedure based on BM3D denoising. Right: corresponding estimation errors. Note how both of the comparison methods create strong artifacts around the areas with the highest contrast, as pointed by the arrows. These artifacts are which are method artifacts present only in the results by these two algorithms.

streaks, although they are generally more intense towards the edges of the projections due to weak photon flux and Poisson noise affecting the bright-field. Thus, the *Fly* benefits greatly from both the extreme streak removal procedure of Section 3.4 and relaxing the stationarity assumption by performing PSD estimation and denoising in multiple parts for each sinogram as described in Section 3.3.3. The denoising results of two different sinograms are shown in Figure 12; the corresponding tomograms of the second sinogram of Figure 12 are shown in Figure 13.

We also test the algorithm on a soft tissue sample *00076* displaying severe ring artifacts freely available in TomoBank (De Carlo *et al.*, 2018). The data contains 2000 projections with $2.2 \mu\text{m}$ pixels, 100ms exposure time obtained at the Advanced Photon Source, 2-BM beamline; other experimental parameters are X-ray energy of 60-70 keV, 10um LuAG Scintillator, and sample-to-detector distance as 90mm. The sinograms are 2560px in width. Included are ten samples for bright- and dark-fields, which are averaged to obtain a single bright-field and dark-field. The denoising results of a single sinogram are shown in Figure 14, and the corresponding tomograms in Figure 15.

4.1. Implementation details

We use the BM3D implementation for Python (available from the PyPI package *bm3d*) with the 'refilter' profile and input PSD estimated as described in Section 3.3.2.

For the multiscale denoising procedure, we performed vertical binning with $m_v = \lceil m/m/64 \rceil \approx 64\text{px}$; this value, being slightly larger than the height of the BM3D search neighborhood of Section 2.2.1 ($39 \times 39\text{px}$), allows our method to attenuate streaks which change slowly across the angle – a larger value of m_v might be used to deal with streaks featuring faster variation. The number of horizontal scales K for each sinogram was set as $K = \lfloor \log_2(n/40) \rfloor$, which gives $K = 3$ for *Fly* and the Shepp-Logan phantom, and $K = 6$ for *00076*; these values offer a compromise between denoising wide streaks versus preserving low-frequency signal components – larger values of K not only result in Z_K narrower than the BM3D search neighborhood, but also in extremely coarse scales that naturally feature a very high SNR that may lead to overestimating ς_K and hence to over-smoothing. For the localized processing of each scale (Section 3.3.3), we estimate ς_k , $K \geq k \geq 0$ and apply BM3D denoising on 39-pixel wide segments, following the width of BM3D search neighborhood. For the attenuation of extreme streaks, we used a $19 \times 19\text{px}$ window.

To consider the computational cost, we note that the full denoising process of *Fly* ($181 \times 512 \times 512\text{px}$) run single-threaded on *AMD Ryzen 7 1700* processor takes about one hour, mostly due to the BM3D denoising in CPU. A highly parallel GPU-based implementation is expected to reduce this runtime to the scale of seconds (Davy & Ehret, 2020). The complexity of BM3D is linear with the number of pixels in the noisy image. Thus, the computation time is directly proportional to the sinogram height after vertical binning. As each iteration of the horizontal multiscale denoising halves the number of pixels, the computational cost of BM3D for an extra iteration $k > 0$ is then

$1/2^k$ th of the cost of $k=0$, the total for all $k=0, \dots, K$ being at most twice that of single scale denoising of Z_0 .

The correlation kernels g_c and g_B do not depend on the input or scale, and can thus be pre-computed. To compute g_B , we use directly the definition (23) through a Monte Carlo simulation of sample standard deviation in Fourier domain. We note that as the kernel is vertically constant, it suffices to perform this simulation in 1-D and repeat the kernel m_v times in the vertical dimension.

For Münch *et al.* (2009) and Vo *et al.* (2018), we use implementations *remove_stripe_fw* and *remove_all_stripe* provided by the *tomopy* Python library of Gürsoy *et al.* (2014). The tomograms of each experiment are reconstructed using the *xpack* library (Marchesini *et al.*, 2020).

5. Discussion and conclusions

We have presented a model for streak noise in sinogram domain as locally stationary correlated noise additive in logarithmic scale. Based on this model, we have described a BM3D-based multiscale denoising procedure removing streak noise, and consequently, the tomogram ring artifacts. The use of the recently proposed variant (Mäkinen *et al.*, 2020) of BM3D is crucial for this work, as we deal with long-range noise correlation which earlier BM3D designs could not handle satisfactorily.

Tested on both synthetic and real data, our denoising procedure achieves state-of-the-art performance in streak removal. Compared to the two popular streak removal algorithms Münch *et al.* (2009) and Vo *et al.* (2018), our procedure achieves superior results both visually and quantitatively in terms of signal-to-noise ratio. Although all tested algorithms manage to successfully remove most streak noise, both Münch *et al.* (2009) and Vo *et al.* (2018) tend to create large distortions especially where the intensities of the underlying sinogram columns vary significantly. This type of artifact hinders interpretation of the results and subsequent analysis such as segmentation. In comparison, the proposed algorithm offers similar or better streak removal without further distorting the sinogram.

The proposed multiscale framework, here using basic pixel binning and debinning, could be extended to more sophisticated scale decompositions, such as steerable pyramids, contourlets, or dual-tree wavelets (Kovacevic & Chebira, 2008). In this work, we have considered each sinogram as a separate input for BM3D for simplicity, but the same mechanism can be used for simultaneous filtering of the entire 3-D stack of sinograms. In this way, the similarities between consecutive sinograms of the stack could be utilized within the collaborative filter.

As the sinograms are commonly processed after a logarithmic transform, we have not discussed inversion of the logarithm needed for denoising. Although the exponential function is naturally the inverse of the logarithm, the nonlinearity of the logarithm causes bias in a denoised sinogram if inverted this way. Hence, if the sinogram should be reverted back from the logarithmic domain after denoising, an exact unbiased inverse (Mäkitalo & Foi, 2010; Mäkitalo *et al.*, 2010) should be used instead.

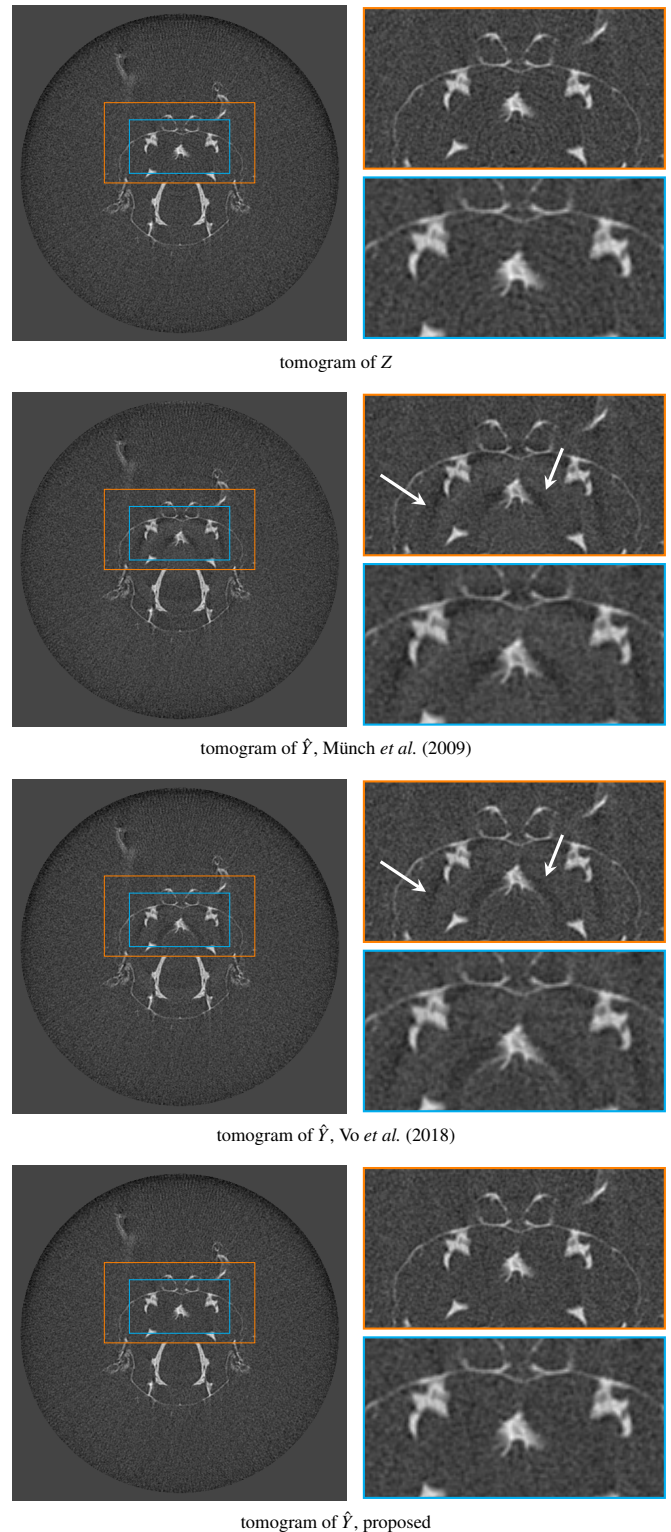
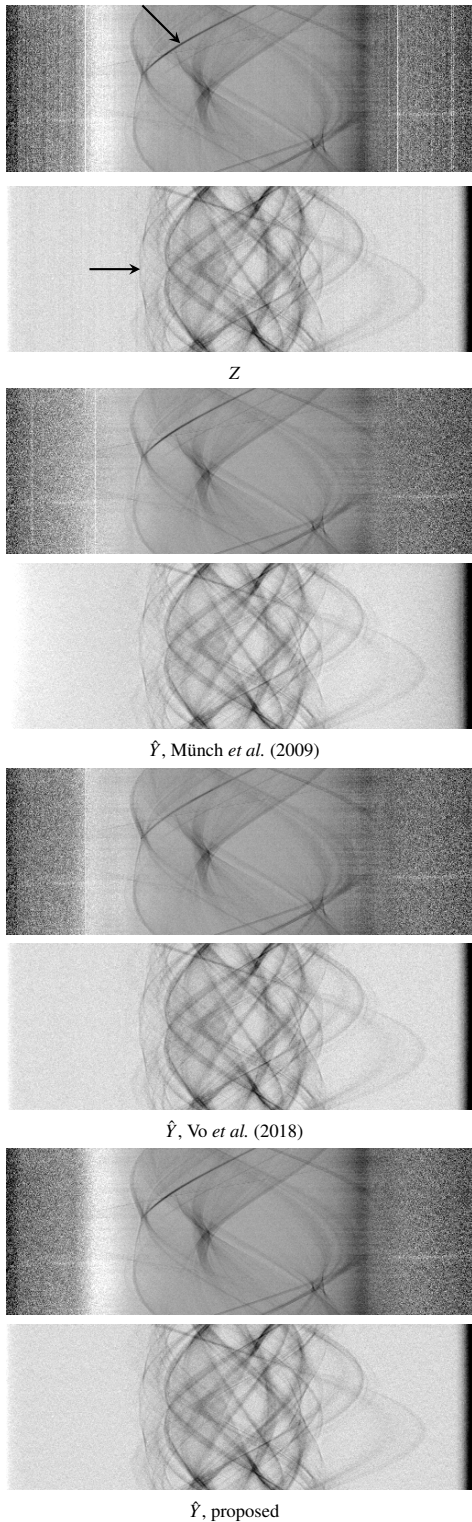


Figure 12

Comparison of two sinograms of *Fly* after different denoising procedures. Top to bottom: noisy sinogram Z , Münch *et al.* (2009), Vo *et al.* (2018), proposed procedure based on BM3D denoising. Although Vo *et al.* (2018) is very effective at removing streaks, it also considerably affects the sinogram features; note, for example, the considerably weaker bold diagonal line (indicated by the first arrow) compared to the other algorithms. Both Münch *et al.* (2009) and Vo *et al.* (2018) also distort larger areas of the sinograms, as pointed out by the second arrow; these problems are absent from the BM3D-based result. Although not visually obvious here, the differences cause severe artifacts in the tomograms, as can be seen in Figure 13.

Figure 13

Comparison of resulting tomograms after different denoising procedures on the second sinogram of *Fly* shown in Figure 12. Top to bottom: noisy reconstructed object, Münch *et al.* (2009), Vo *et al.* (2018), proposed procedure based on BM3D denoising. Although all methods achieve good results in removing the streaks, both Münch *et al.* (2009) and Vo *et al.* (2018) introduce strong shadows absent from the proposed estimate, as indicated by the arrows.

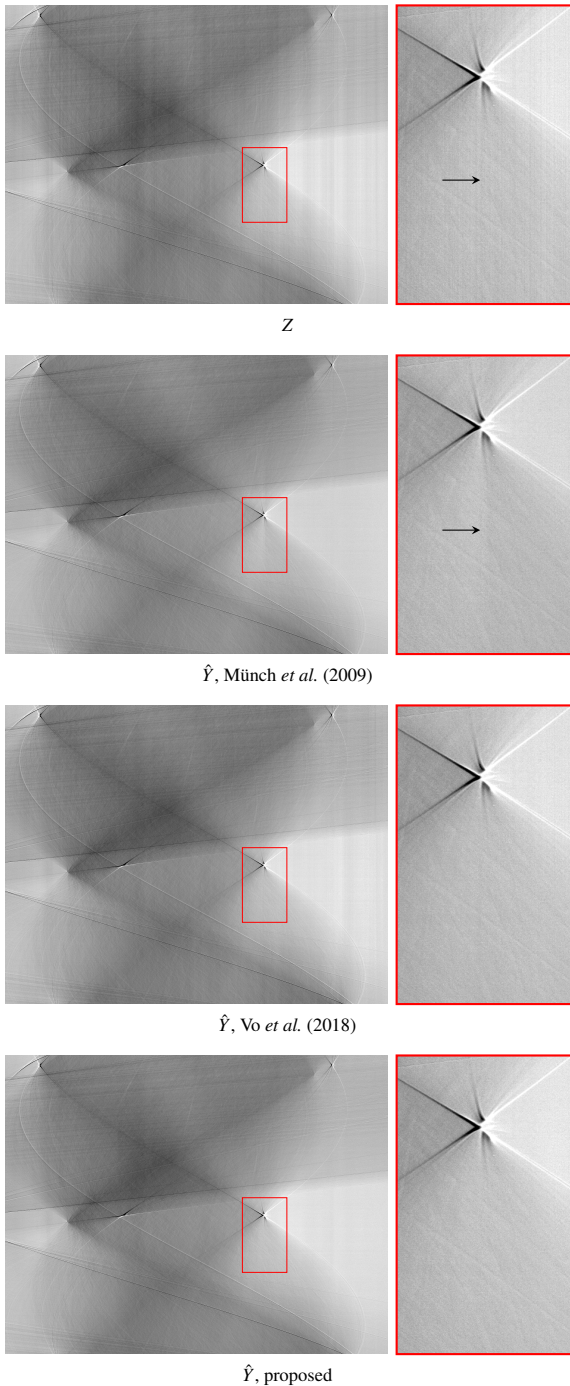


Figure 14

Comparison of sinograms after different denoising procedures on 00076. Top to bottom: noisy sinogram Z , Münch *et al.* (2009), Vo *et al.* (2018), proposed procedure based on BM3D denoising. Note how in the zoom in, the proposed method manages to remove streak noise without creating additional artifacts. Münch *et al.* (2009) creates a horizontal streak-like artifacts as seen in the middle of the zoom-in, not present in the noisy sinogram; Vo *et al.* (2018) does not fully denoise the sinogram.

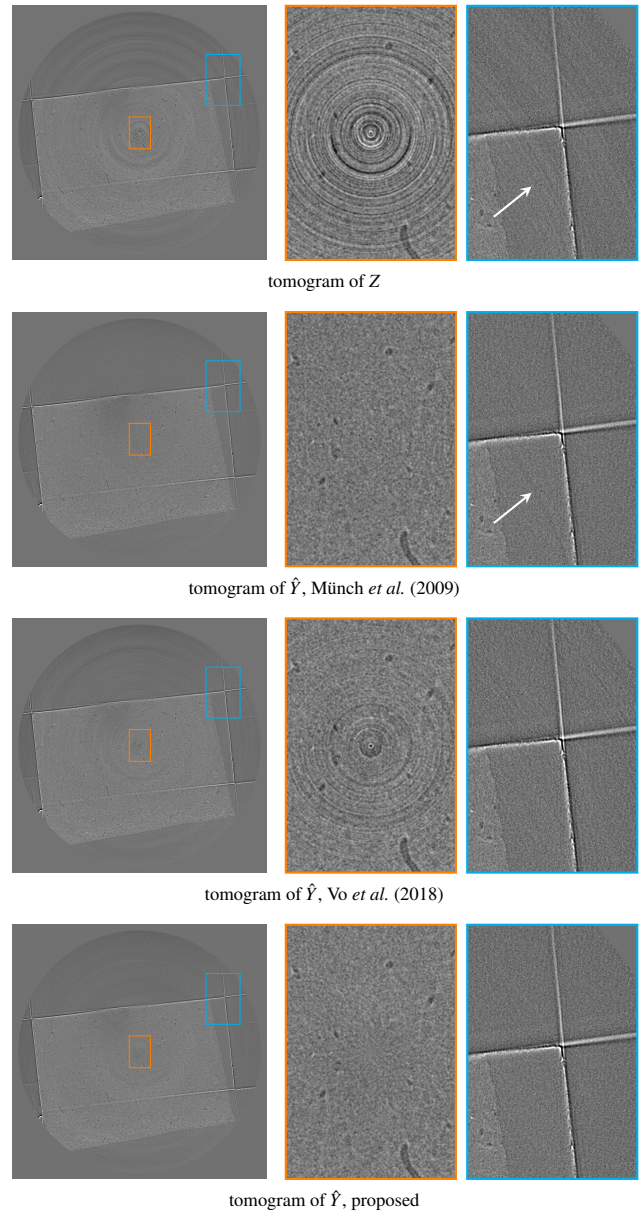


Figure 15

Comparison of resulting tomograms after different denoising procedures on 00076. Top to bottom: noisy reconstructed object, Münch *et al.* (2009), Vo *et al.* (2018), proposed procedure based on BM3D denoising. Münch *et al.* (2009) manages to remove almost all noise in both low and high frequencies, but creates artifacts where the original did not have any, as seen from the rightmost zoom. The proposed denoising procedure removes most of the noise (including the wide streaks still present in Vo *et al.* (2018)), and does not introduce further artifacts. Note also the central pixel, magnified in the middle, which is very dark for both Münch *et al.* (2009) and Vo *et al.* (2018), whereas the proposed procedure does not leave any visible artifact.

Acknowledgements

We are very thankful to Dr. Sheraz Gul of Sigray Inc. for providing us with the experimental Fly data. This work was supported by the Academy of Finland (project no. 310779) and Sigray Inc.

References

Anas, E. M. A., Lee, S. Y. & Hasan, M. K. (2010). *Phys. Med. Biol.* **55**(22), 6911.

-
- Artul, S. (2013). *BMJ Case Reports*, **2013**.
- Azzari, L. & Foi, A. (2016). *IEEE Signal Proc. Let.* **23**(8), 1086–1090.
- Boas, F. E. & Fleischmann, D. (2012). *Imaging Med.* **4**(2), 229–240.
- Croton, L. C., Ruben, G., Morgan, K. S., Paganin, D. M. & Kitchen, M. J. (2019). *Opt. Express*, **27**(10), 14231–14245.
- Dabov, K., Foi, A., Katkovnik, V. & Egiazarian, K. (2007). *IEEE Trans. Image Process.* **16**(8), 2080–2095.
- Dabov, K., Foi, A., Katkovnik, V. & Egiazarian, K. O. (2008). In *Proc. SPIE Electronic Imaging 2008*, no. 681207.
- Davidson, D., Fröjdh, C., O’Shea, V., Nilsson, H.-E. & Rahman, M. (2003). *Nucl. Instrum. Meth. A*, **509**(1-3), 146–150.
- Davy, A. & Ehret, T. (2020). *J. Real-Time Image Process.* pp. 1–18.
- De Carlo, F., Gürsoy, D., Ching, D. J., Batenburg, K. J., Ludwig, W., Mancini, L., Marone, F., Mokso, R., Pelt, D. M., Sijbers, J. *et al.* (2018). *Meas. Sci. Technol.* **29**(3), 034004.
- Gürsoy, D., De Carlo, F., Xiao, X. & Jacobsen, C. (2014). *J. Synchrotron. Radiat.* **21**(5), 1188–1193.
- Haibel, A. (2008). *Advanced Tomographic Methods in Materials Research and Engineering*, pp. 141–160.
- Hampel, F. R. (1974). *J. Am. Stat. Assoc.* **69**(346), 383–393.
- Jha, A. K., Purandare, N. C., Shah, S., Agrawal, A., Puranik, A. D. & Rangarajan, V. (2013). *Indian J. Nucl. Med.* **28**(4), 232.
- Kovacevic, J. & Chebira, A. (2008). *An introduction to frames*. Now Publishers Inc.
- Mäkinen, Y., Azzari, L. & Foi, A. (2020). *IEEE Trans. Image Process.* **29**, 8339–8354.
- Mäkitalo, M. & Foi, A. (2010). *IEEE Trans. Image Process.* **20**(1), 99–109.
- Mäkitalo, M., Foi, A., Fevraleev, D. & Lukin, V. (2010). In *2010 Int. Conf. Math. Meth. Electromag. Th.*
- Marchesini, S., Trivedi, A., Enfedaque, P., Perciano, T. & Parkinson, D. (2020). In *Computational Science – ICCS 2020*, edited by V. V. Krzhizhanovskaya, G. Závodszy, M. H. Lees, J. J. Dongarra, P. M. A. Sloot, S. Brissos & J. Teixeira, pp. 248–261. Cham: Springer International Publishing.
- Münch, B., Trtik, P., Marone, F. & Stapanoni, M. (2009). *Opt. Express*, **17**(10), 8567–8591.
- Paleo, P. & Mirone, A. (2015). *J. Synchrotron. Radiat.* **22**(5), 1268–1278.
- Pelt, D. M. & Parkinson, D. Y. (2018). *Measurement Science and Technology*, **29**(3), 034002.
- Seibert, J. A., Boone, J. M. & Lindfors, K. K. (1998). In *P. Soc. Photo-Opt. Ins.*, vol. 3336, pp. 348–354.
- Swinehart, D. F. (1962). *J. Chem. Educ.* **39**(7), 333.
- Vidal, F. P., Létang, J. M., Peix, G. & Cloetens, P. (2005). *Nucl. Instrum. Meth. B*, **234**(3), 333–348.
- Vo, N. T., Atwood, R. C. & Drakopoulos, M. (2018). *Opt. Express*, **26**(22), 28396–28412.
-